RESEARCH ARTICLE | FEBRUARY 01 2024

# Inverse-designed broadband low-loss grating coupler on thick lithium-niobate-on-insulator platform *⊙*

Yijun Xie <sup>(i)</sup>; Mingming Nie <sup>(i)</sup>; Shu-Wei Huang **∑** <sup>(i)</sup>



Appl. Phys. Lett. 124, 051108 (2024) https://doi.org/10.1063/5.0184413







# An innovative I-V characterization system for next-gen semiconductor R&D

Unique combination of ultra-low noise sourcing + high-sensitivity lock-in measuring capabilities





# Inverse-designed broadband low-loss grating coupler on thick lithium-niobate-on-insulator platform

Cite as: Appl. Phys. Lett. **124**, 051108 (2024); doi: 10.1063/5.0184413 Submitted: 8 November 2023 · Accepted: 15 January 2024 · Published Online: 1 February 2024









## **AFFILIATIONS**

Department of Electrical, Computer, and Energy Engineering, University of Colorado Boulder, 425 UCB, Boulder, Colorado 80309, USA

### **ABSTRACT**

A grating coupler on 700-nm-thick Z-cut lithium-niobate-on-insulator platform with high coupling efficiency, large bandwidth, and high fabrication tolerance is designed and optimized by inverse design method. The optimized grating coupler is fabricated with a single set of ebeam lithography and etching process, and it is experimentally characterized to possess peak coupling efficiency of  $-3.8 \, \text{dB}$  at 1574.93 nm, 1 dB bandwidth of 71.7 nm, and 3 dB bandwidth of over 120 nm, respectively.

Published under an exclusive license by AIP Publishing. https://doi.org/10.1063/5.0184413

Lithium niobate (LN) is a widely used material across disciplines due to its large refractive index, large transparency window, high second-  $(\chi^{(2)})$  and third-  $(\chi^{(3)})$  order nonlinearities, as well as its excellent electro-optic (EO) property. The recently developed lithium-niobate-on-insulator (LNOI) platform has brought new vigor and vitality to integrated photonics, which creates more opportunities for better performance and lower power consumption in various applications such as atomic clock, frequency synthesizer, LIDAR, and OCT-based bioimaging. These integrated devices are mainly demonstrated on thick LNOI platforms, with thickness ranging from 600 to 800 nm, where modes can be strongly confined and dispersion can be flexibly engineered.  $^{2-9}$ 

As for real-world applications, input and output couplers that are compatible with such integrated LNOI devices can help further improve the performance in different ways. Couplers with high coupling efficiency are essential to deliver high on-chip power for efficient nonlinear applications such as second harmonic generation and EO modulation.<sup>2–4</sup> Highly efficient couplers are critical for chip-scale quantum applications that demand low loss. Broadband couplers provide capability of retaining the spectral information and the accommodation of tunability for those broadband applications such as supercontinuum generation, femtosecond pulse generators, quadratic/ Kerr combs/soliton generation and tunable lasers.<sup>5–9</sup> Therefore, couplers on such thick LNOI platforms with not only high coupling

efficiency but also large bandwidth are fundamentally important to fulfill the potential of those integrated LNOI devices.

Compared to the edge coupler requiring end-facet dicing, polishing, and additional customized lensed fiber, grating coupler (GC) provides high coupling efficiency with great placement flexibility. More importantly, GCs can be used along with fiber arrays, which is convenient for multi-device testing and operation and thereby offers compelling advantages for high-volume production. Conventionally, GCs with uniform periodicity and filling factor of the grating structures can only provide limited coupling efficiency with a narrow bandwidth. Efforts such as adding bottom reflector to enhance the directionality of the power going upward and patterning overlay structure with higher refractive index or metal have been made to improve the performance of the GCs. 10-19 These techniques, however, compromise the compatibility of the GC with other thick LNOI devices and impair the device quality. Introducing linear apodization and chirping where the periodicity and duty cycle vary linearly has been proven effective in improving the performance without any additional structure manipulations.<sup>20</sup> Nevertheless, compared to the optimization of GC on a thin LNOI platform, the deep etching required for the GC on a thick LNOI platform not only imposes nanofabrication challenges but also limits the choice of GC apodization and chirping factors due to the unavoidable base angle, which renders optimization with poor quality. The best GC compatible with the thick LNOI devices that has been experimentally

a) Electronic mail: yijun.xie@colorado.edu

b) Author to whom correspondence should be addressed: shuwei.huang@colorado.edu

demonstrated so far exhibits only  $-6.3\,\mathrm{dB}$  peak coupling efficiency with  $1\,\mathrm{dB}$  bandwidth and  $3\,\mathrm{dB}$  bandwidth of 40 and  $90\,\mathrm{nm}$ , respectively.  $^{21}$ 

In contrast to forward design method where only limited parameter space is explored to provide provisional optimization, inverse design method based on the gradient descent algorithm has been demonstrated on other platforms in recent years as a more advanced and effective method to provide comprehensive optimization on the figure of merit (FOM), which is defined usually as the overall coupling efficiency in a given bandwidth, by updating the structure iteratively according to the gradient of FOM in much expanded parametric space.<sup>22</sup> In this work, we introduce the inverse design method to the thick LNOI GC and incorporate several additional steps to ensure a good match between the design and the experiment. We first characterize the base angle of fabricated GC grooves in the test run and take it into consideration in the optimization routine, improving the fidelity of the fabricated device. Subsequently, we enforce that the GC only consists of strip grooves with the characterized base angle and equal etching depth to avoid abstract geometries and multiple patterning and etching processes.<sup>23,24</sup> Furthermore, we include a hard constraint on the minimal feature size to make sure that the optimized GC does not impose excessive nanofabrication challenges.<sup>23</sup> Our final design is based on a 700 nm-thick Z-cut LNOI platform with −2.94 dB peak coupling efficiency at 1572.4 nm, 1 dB bandwidth of 69 nm, and 3 dB bandwidth of 113 nm from the fundamental transverse electric (TE) mode input of a single mode fiber at telecom band (SMF-28), which has comprehensive improvement compared to the forward design. The proposed GC is subsequently fabricated on a 700-nm-thick Z-cut LNOI chip and experimentally characterized with  $-3.8 \, \mathrm{dB}$  peak coupling efficiency at 1574.9 nm, 1 dB bandwidth of 71.7 nm, and 3-dB bandwidth of over 120 nm, which agrees well with the designed performance. We believe the proposed GC that is perfectly compatible with those integrated devices can benefit various emergent applications.

We start the initial optimization with sweeping apodization and filling factors, after which initial design is found for further optimization, and the initial design is further optimized using inverse design method by iteratively adjusting the widths of each grating pillar and trench independently. The length of the grating pillars l is fixed at 12  $\mu$ m to match the mode from SMF-28 along the out-of-plane direction (y). Due to the large aspect ratio of the grating pillars, they can be considered as infinitely long slab waveguide along y direction so that the simulation result from three-dimension finite-difference time-domain (3D FDTD) method (Lumerical, Ansys) is almost identical to the result given by two-dimension FDTD (2D FDTD) method. Therefore, 2D FDTD method is chosen for all the simulations throughout the design and optimization section in the consideration of time and computational resources saving.

Some general parameters of the GC are kept as constants throughout the design section (unless otherwise stated): the number of periods is chosen to be 15, and the last period ends with a straight waveguide with a width of 6  $\mu$ m, the total thickness of LN h and the etched depth e are 700 and 450 nm, respectively. The base angle of the grating along the light propagation direction (x) is set to be 70° based on our estimation from the SEM measurement, while the base angle along y direction is neglected. SMF-28 is located always at the center of the GC along the y direction and around 2.5  $\mu$ m above the top surface of the GC along the z direction.

The schematic of the simulation is shown in Fig. 1. In order to obtain good initial condition for further optimization by inverse design, we first introduce linear apodization and the chirped grating period to the GC whose periods  $(\Lambda_i)$  and filling factors  $(F_i)$  of the gratings are given by the following equations:

$$\Lambda_i = \frac{\lambda_c}{a + b \times F_i},\tag{1}$$

$$F_{i+1} = F_1 - R \times x_i, \tag{2}$$

in which  $F_1$  is the filling factor of the first grating period that is fixed at 0.35, R is the apodization factor that is fixed at 0.01/ $\mu$ m,  $x_i$  is the end of the current grating, and  $\lambda_c$  is the central wavelength that is set to be 1575 nm for better spectral coverage across the telecom C and L bands. For each period, the GC starts at x=0 with the etched trench followed by the grating pillar and the width of the trench  $t_i$  and the grating  $w_i$  are given by  $\Lambda_i - w_i$  and  $\Lambda_i \times F_i$ , respectively. The initial optimization is conducted by sweeping unitless parameters a and b with the sweep of the a position of the SMF-28 a and the angle a0 of the SMF-28 with respect to normal direction of the GC (a2) for each pair of a3 and a4. The optimized design is selected with peak coupling efficiency a4.48 dB at central wavelength 1571 nm, 1 and 3 dB bandwidths of 34 and 84 nm, respectively, and the GC parameters are listed in Table I.

GC above-illustrated, as the initial condition, is further optimized by inverse design method. Full degrees of freedom on the width of each grating pillar  $w_i$  and trench  $t_i$  are granted while the x position  $d_f$  and the angle  $\theta$  of the fiber, the length of the gratings l, and the etched depth e remain fixed to be 7  $\mu$ m,  $6^{\circ}$ , 12  $\mu$ m, and 450 nm, respectively. FOM is defined as the negative value of the average coupling efficiency in the wavelength range of 1555–1595 nm as expressed in the following equation:

$$FOM = -\frac{\sum_{i=1}^{N} CE_i}{N}, \qquad (3)$$

where  $CE_i$  stands for the coupling efficiency at the reference wavelength. N is the number of reference wavelengths, which is set to be 51 so that the transmission data are recorded every 0.8 nm. Moreover, the constraint of the minimal feature size of 150 nm is added to avoid any super small structure that will impose excessive challenge on fabrication, and the stopping criteria are set to be FOM equals -0.5. To start

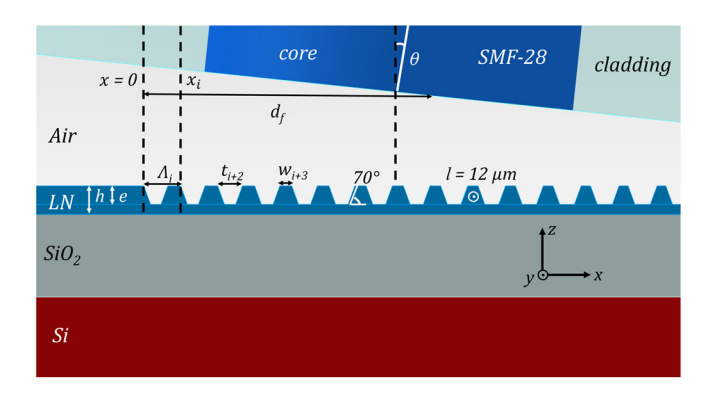


FIG. 1. 2D Schematics of the grating coupler simulation.

**TABLE I.** Parameters of the optimized GC with linear apodization and chirping and the SMF-28.

$\overline{F_0}$	а	b	$R\left(\mu\mathrm{m}^{-1}\right)$	$d_f (\mu m)$	$\theta$ (deg)
0.35	1.75	0.02	0.01	7	6

with, FOM of the initial design is calculated by 2D FDTD simulation. Then the gradient of FOM with respect to each grating pillar and trench will be evaluated by adjoint method, which allows fast gradient evaluation regardless of the number of parameters by only two FDTD simulations, if the stopping criterion is not satisfied. All the widths will be then updated accordingly by the minimizer, and FOM of the updated structure will be calculated iteratively. Eventually, the iteration will end once the stopping criterion is met or minimal FOM is found, and the updated widths of each grating pillar and trench will be provided along with the optimal FOM as illustrated in Fig. 2. The widths of gratings and trenches of the optimized GC are given in Table II.

By sweeping the x position  $d_f$  and the angle  $\theta$  of the SMF-28, the optimal position of the SMF-28 is subsequently found to be 6  $\mu$ m away from the onset of the first trench at 8°, and the performance of  $-2.94\,\mathrm{dB}$  peak coupling efficiency at 1572.4 nm, 1-dB bandwidth of 69 nm, and 3-dB bandwidth of 113 nm from the fundamental TE mode input of the SMF-28 is predicted. As listed in Table II, there is no super small structure determined by the constraint or any structure with irregular shape existing in the proposed GC.

In order to investigate the fabrication tolerance of the proposed GC, the variation of the peak coupling efficiency and 1-dB bandwidth are calculated with etched depth e ranging from 400 to 500 nm and base angle fixed at 70°, and with base angle varying from 60° to 80° and etched depth e fixed at target value 450 nm in the consideration that different etching tools and recipes might render different base angles of the gratings. Furthermore, the random dimension variations from  $\pm 1\%$  to  $\pm 5\%$  from the designed values, which is common for electron beam (E-beam) lithography process, are also introduced to the size of each trench width  $t_i$  and grating width  $w_i$  separately, while

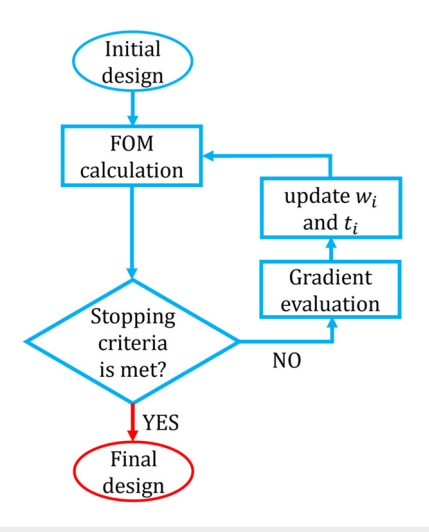


FIG. 2. Flow chart of the inverse design method.

TABLE II. Parameters of the optimized GC by inverse design.

	$t_1$	$t_2$	$t_3$	$t_4$	$t_5$	$t_6$	$t_7$	$t_8$
Trench size (nm)	285 t <sub>9</sub>	542 t <sub>10</sub>	859 t <sub>11</sub>	726 t <sub>12</sub>	684 t <sub>13</sub>	681 t <sub>14</sub>	685 t <sub>15</sub>	670
	$601 \\ w_1$	678 w <sub>2</sub>	634 w <sub>3</sub>	644 w <sub>4</sub>	606 w <sub>5</sub>	659 w <sub>6</sub>	722 w <sub>7</sub>	$w_8$
Grating size (nm)	302 w <sub>9</sub>	157 w <sub>10</sub>	161 w <sub>11</sub>	230 w <sub>12</sub>	272 w <sub>13</sub>	248 w <sub>14</sub>	257 w	295 '15
	253	280	252	210	196	175	60	000

the etched depth e and the base angle are both set to be the target values to evaluate how random dimension variations affect the performance of the optimized GC. The results are obtained from 100 individual simulations for each level of variation. The effects of different etched depths, base angles, and the random dimension variations on peak coupling efficiency, and 1-dB bandwidth are shown in Figs. 3(a) and 3(b), Figs. 3(c) and 3(d), and Figs. 3(e) and 3(f), respectively.

As shown in Figs. 3(a) and 3(b), the peak coupling efficiency of the GC varies from -3.9 to -2.85 dB, while the 1-dB bandwidth varies from 66 to 82 nm in the exact opposite trend when the base angle is fixed at  $70^{\circ}$ . The performance of the proposed GC remains consistent when the base angle of the gratings varies from  $65^{\circ}$  to  $75^{\circ}$  when the etched depth e is kept at 450 nm as illustrated in Figs. 3(c) and 3(d). However, the peak coupling efficiency starts to decay severely to -3.8 dB as the base angle approaches  $80^{\circ}$ , while the 1-dB bandwidth gets narrowed down by around 6 nm as the gratings get flatter.

On the other hand, the performance of the proposed GC is not prone to the random dimension variations as depicted in Figs. 3(e) and 3(f). There is only about 0.3 dB peak coupling efficiency, and 8 nm 1-dB bandwidth reduction, respectively, for the most extreme cases where the random dimension variation is  $\pm 5\%$  for the size of each trench and grating pillar, which indicates the overall high fabrication tolerance of the proposed GC.

The proposed GC is fabricated on a 1 cm<sup>2</sup> 700-nm-thick Z-cut LNOI chip (NanoLN). After thoroughly cleaning the chip, a 1.2- $\mu$ mthick layer of AR-P 6200 (Allresist) is spin-coated and baked at 180 °C for 2 min. An E-beam lithography is conducted using JEOL JBX-6300 fs to define the soft mask and a subsequent argon ion milling is conducted for 12 min and 40 s to achieve the etched depth of 450 nm. After the residual mask is removed by remover PG, the LNOI chip is soaked in RCA solution (1:1:5 of H<sub>2</sub>O<sub>2</sub>, NH<sub>4</sub>OH, and DI water) overnight at room temperature for the re-deposition removal to reduce the sidewall roughness. Each device consists of a 100-μm-long straight waveguide with the top width of 1.8  $\mu$ m, two 300- $\mu$ m-long tapers with the top width adiabatically expanding from 1.8 to 12  $\mu m$  on both sides, and two proposed GCs. For the comparison of the performance of the GC before and after the inverse design optimization, two GCs before the inverse design optimization with the exact same waveguide and tapers are also fabricated on the same chip. SEM images of the optimized GC by inverse design method are shown in Fig. 4.

For the coupling efficiency characterization, two SMF-28s are cleaved and clamped by fiber holders that are mounted on rotational

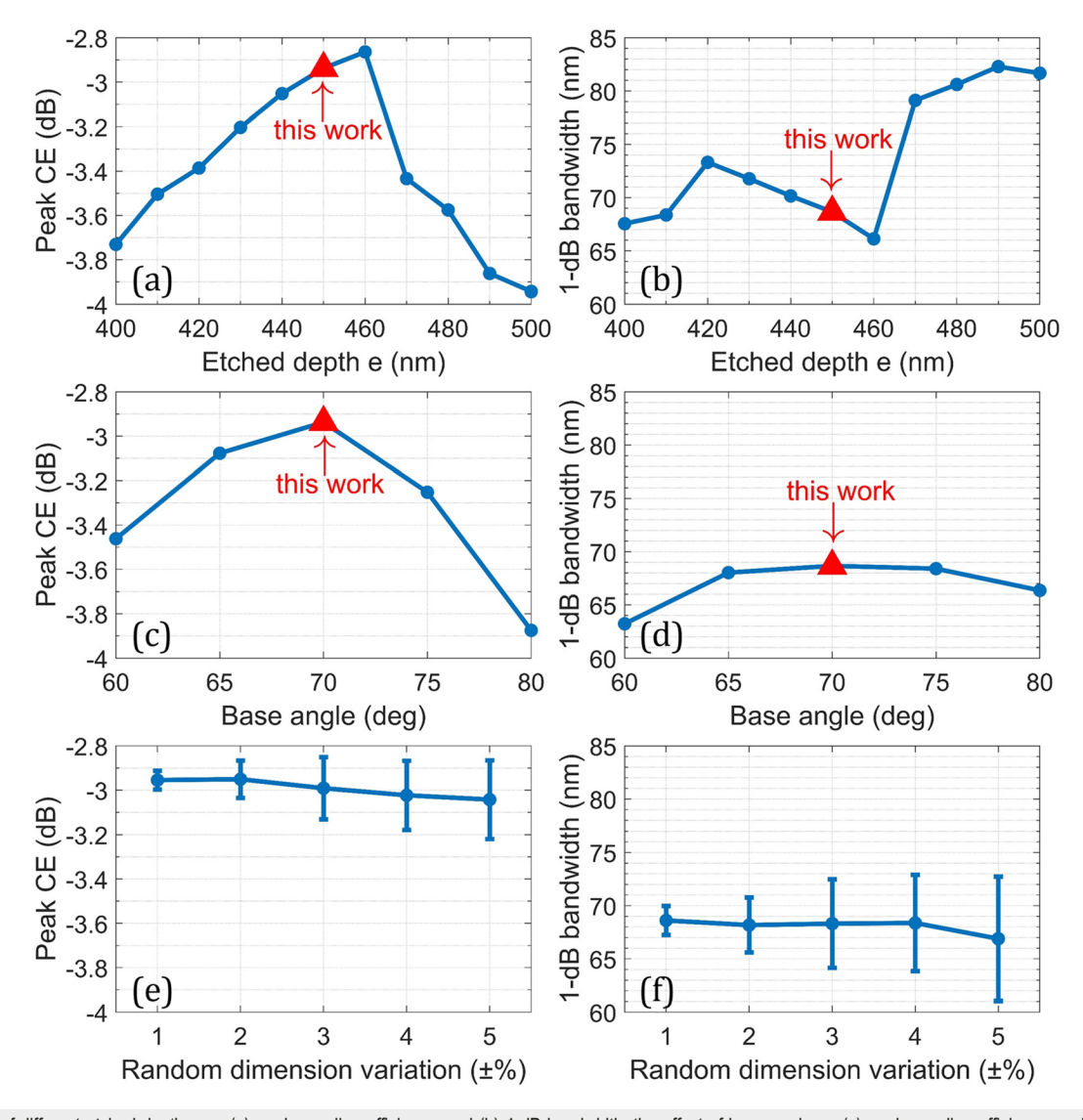


FIG. 3. Effect of different etched depth e on (a) peak coupling efficiency, and (b) 1-dB bandwidth; the effect of base angle on (c) peak coupling efficiency, and (d) 1-dB bandwidth; and the effect of random dimension variation on (e) peak coupling efficiency, and (f) 1-dB bandwidth.

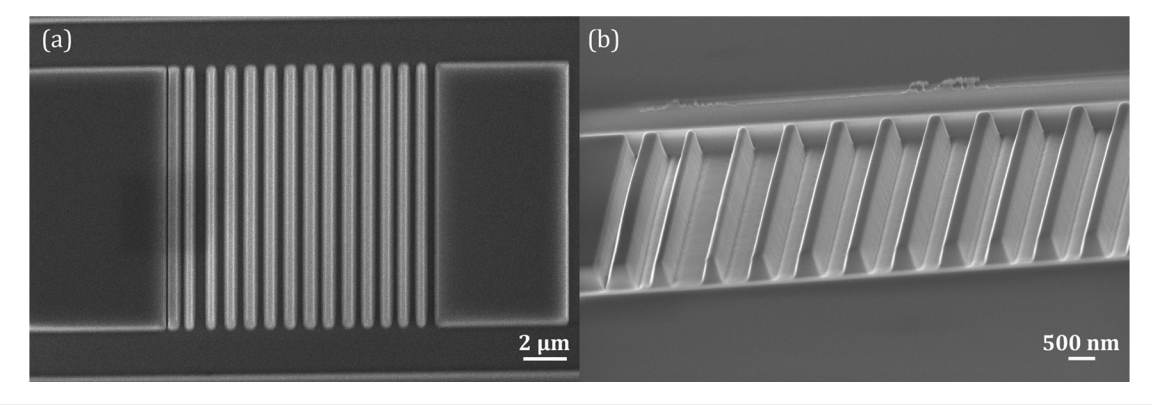
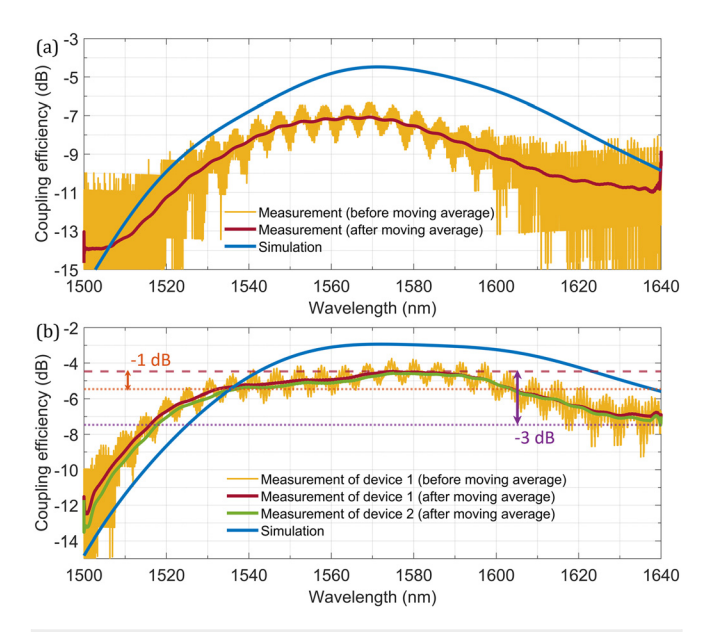


FIG. 4. SEM images of the fabricated GC: (a) top view and (b) side view.



**FIG. 5.** Simulated and measured coupling efficiency of (a) the GC with linear apodization and chirping and (b) the GCs optimized by inverse design method.

stages so that the fibers can be adjusted to the desired angle with respect to the normal direction of the GCs. Rotational stages are subsequently fixed onto three-axis translation stages, which are placed on the opposite side of the fabricated device. A polarization controller connects the input SMF-28 and the tunable laser input from Santec TSL-710, while the output SMF-28 is connected to a photodetector whose output signal is collected by a digitizer (CSE1222 Razor Express, Gage) with 100 Ks/s sampling rate for the data acquisition. Santec is continuously scanned from 1500 to 1640 nm at 100 nm/s scan rate with 5 dBm nominal optical output power. The acquired data are converted to optical power by electrical-optical signal conversion and calibration and then the coupling efficiency of the GC can be further extracted. The simulated and the measured coupling efficiency after the moving average process of the GC with linear apodization and

chirping, and two GCs optimized by inverse design are illustrated in Figs. 5(a) and 5(b), respectively.

As shown in Fig. 5(a), the GC with linear apodization and chirped grating period has similar performance compared to the simulation results with 1-dB bandwidth of 45.7 nm and 3-dB bandwidth of 85.8 nm except for the peak coupling efficiency. The measured peak coupling efficiency is -6.33 dB ( $-7.1 \pm 0.77$  dB from the moving average process) at 1569.3 nm with almost  $-2 \, dB$  difference from the simulation result, and we attribute this discrepancy mainly to the fabrication imperfection due to the proximity of this device to the edge of the chip. Compared to the results of the GC with the linear apodization and chirped grating period, the performance of the GC has been comprehensively improved after optimization by inverse design method with the peak coupling efficiency, which so red from -6.33 to  $-3.8 \, \mathrm{dB} \, (-4.5 \pm 0.7 \, \mathrm{dB} \, \mathrm{from} \, \mathrm{the} \, \mathrm{moving} \, \mathrm{average} \, \mathrm{process}), \, 1 \, \mathrm{dB} \, \mathrm{band}$ width expanded from 45.7 to 71.7 nm, and 3-dB bandwidth, from 85.8 nm to over 120 nm, respectively, as plotted in Fig. 5(b). The interference fringes in the transmission spectrum are majorly contributed by the backreflection from the Fabry-Pérot (FP) cavity formed by the configuration of two GCs at both ends of the device. The reflection is as low as  $-18 \, dB$  inside the wavelength range of our interest, while it goes up to  $-10 \, dB$  at longer wavelength, which is in the same level as the results reported in recent work.<sup>18</sup> In addition, the measured results of the GC by inverse design match well with the simulation results with even slightly larger bandwidths but lower peak coupling efficiency, which can be explained by the random dimension variations of grating structures as discussed earlier. Two fabricated GCs have similar performance as shown in the red and green curves in Fig. 5(b), which further validates the high tolerance of the optimized GC on the random dimension variations of the grating structures.

In summary, a GC on 700-nm-thick Z-cut LNOI with high coupling efficiency and large bandwidth is proposed and optimized by inverse design method, and the optimized GC is fabricated with only a single set of E-beam lithography and etching process. Peak coupling efficiency  $-3.8\,\mathrm{dB}$  at central wavelength 1574.9 nm, 1-dB bandwidth 71.7 nm, and 3-dB bandwidth over 120 nm is experimentally demonstrated, in good agreement with the numerical simulation. Comprehensive improvement has been observed in both peak

TABLE III. Performance of the recently demonstrated GCs on LNOI platforms with different thicknesses.

Thickness of LN (nm)	Bottom reflector or overlay patterns?	Etch LN?	Measured peak efficiency (dB)	Measured 1-dB bandwidth (nm)	Measured 3-dB bandwidth (nm)	References
400	Yes	No	-5.82		57	11
400	Yes	No	-3.58			13
400	Yes	No	-3.56			14
400	Yes	No	-2.2		81	15
600	Yes	No	-3.06	55		10
400	Yes	Yes	-0.89	45		18
500	Yes	Yes	-3.5			16
500	Yes	Yes	-1.42			17
300	No	Yes	-3.26		35	19
600	No	Yes	-6.3	${\sim}40$	> 90	20
700	No	Yes	-3.8	71.7	>120	This work

coupling efficiency and bandwidths compared to the initial GC design with linear apodization and chirped grating period.

Table III summarizes the performances of all recently demonstrated LNOI GCs including our inverse-designed GC on thick LNOI platform that exhibits not only high coupling efficiency but also large 1 and 3-dB bandwidths at the same time. Moreover, our inversedesigned GC has high fabrication tolerance without any additional over cladding patterning or the need of bottom reflectors. GC with improved performance on LNOI platform with different crystalline orientations, total thicknesses, or etching depths can also be achieved following the same optimization strategies. One can also target at maximizing bandwidth or manipulating central wavelength by customizing FOM for future research.

Y. Xie thanks L. Rukh, C. Tang, and V. Babicheva for fruitful discussions and A. R. James, J. Nogan, and D. Webb for process advice and N. Prakash, J. Musgrave, and J. Bartos for their help. This work was performed, in part, at the Center for Integrated Nanotechnologies, an Office of Science User Facility operated for the U.S. Department of Energy (DOE) Office of Science by Los Alamos National Laboratory (Contract 89233218CNA000001) and Sandia National Laboratories (Contract DE-NA-0003525) and supported through Grant Nos. NSF OMA 2016244, NSF ECCS 2048202, and ONR N00014-22-1-2224.

# **AUTHOR DECLARATIONS**

### Conflict of Interest

The authors have no conflicts to disclose.

# **Author Contributions**

Yijun Xie: Conceptualization (equal); Data curation (lead); Formal analysis (lead); Investigation (lead); Methodology (lead); Validation (lead); Writing - original draft (lead); Writing - review & editing (equal). Mingming Nie: Data curation (equal); Validation (equal); Writing - review & editing (equal). Shu-Wei Huang: Conceptualization (equal); Formal analysis (equal); Funding acquisition (lead); Project administration (lead); Supervision (lead); Writing review & editing (equal).

## DATA AVAILABILITY

Data underlying the results presented in this paper are not publicly available at this time but may be obtained from the authors upon reasonable request.

# **REFERENCES**

<sup>1</sup>M. Nie, Y. Xie, B. Li et al., "Photonic frequency microcombs based on dissipative Kerr and quadratic cavity solitons," Prog. Quantum Electron. 86, 100437 (2022).

- <sup>2</sup>J.-Y. Chen, C. Tang, Z.-H. Ma et al., "Efficient and highly tunable secondharmonic generation in Z-cut periodically poled lithium niobate nanowaveguides," Opt. Lett. **45**(13), 3789–3792 (2020).

  3J. Lu, J. B. Surya, X. Liu *et al.*, "Periodically poled thin-film lithium niobate
- microring resonators with a second-harmonic generation efficiency of 250,000%/W," Optica 6(12), 1455-1460 (2019).
- <sup>4</sup>C. Wang, M. Zhang, X. Chen et al., "Integrated lithium niobate electro-optic modulators operating at CMOS-compatible voltages," Nature 562(7725), 101-104 (2018).
- <sup>5</sup>M. Yu, B. Desiatov, Y. Okawachi et al., "Coherent two-octave-spanning supercontinuum generation in lithium-niobate waveguides," Opt. Lett. 44(5), 1222-1225 (2019).
- <sup>6</sup>M. Yu, D. Barton III, R. Cheng et al., "Integrated femtosecond pulse generator on thin-film lithium niobate," Nature 612(7939), 252-258 (2022).
- $^{7}$ Y. He, Q.-F. Yang, J. Ling et al., "Self-starting bi-chromatic LiNbO $_{3}$  soliton microcomb," Optica 6(9), 1138-1144 (2019).
- <sup>8</sup>M. Nie and S.-W. Huang, "Quadratic soliton mode-locked degenerate optical
- parametric oscillator," Opt. Lett. **45**(8), 2311–2314 (2020).

  <sup>9</sup>L. Ledezma, A. Roy, L. Costa *et al.*, "Octave-spanning tunable infrared parametric oscillators in nanophotonics," Sci. Adv. **9**(30), eadf9711 (2023).
- <sup>10</sup>J. Jian, P. Xu, H. Chen et al., "High-efficiency hybrid amorphous silicon grating couplers for sub-micron-sized lithium niobate waveguides," Opt. Express 26(23), 29651-29658 (2018).
- <sup>11</sup>Y. Li, X. Huang, Z. Li et al., "Efficient grating couplers on a thin film lithium niobate-silicon rich nitride hybrid platform," Opt. Lett. 45(24), 6847-6850
- <sup>12</sup>X. Ma, C. Zhuang, R. Zeng et al., "Polarization-independent one-dimensional grating coupler design on hybrid silicon/LNOI platform," Opt. Express 28(11), 17113-17121 (2020).
- $^{13}$  Z. Ruan, J. Hu, Y. Xue  $\it et~al.,$  "Metal based grating coupler on a thin-film lithium niobate waveguide," Opt. Express 28(24), 35615-35621 (2020).
- <sup>14</sup>B. Chen, Z. Ruan, K. Chen et al., "One-dimensional grating coupler on lithiumniobate-on-insulator for high-efficiency and polarization-independent coupling," Opt. Lett. 48(6), 1434-1437 (2023).
- 15X. Zhou, Y. Xue, F. Ye et al., "High coupling efficiency waveguide grating cou-
- plers on lithium niobate," Opt. Lett. 48(12), 3267–3270 (2023).

  16I. Krasnokutska, R. J. Chapman, J.-L. J. Tambasco *et al.*, "High coupling efficiency grating couplers on lithium niobate on insulator," Opt. Express 27(13), 17681-17685 (2019).
- 17 S. Kang, R. Zhang, Z. Hao et al., "High-efficiency chirped grating couplers on lithium niobate on insulator," Opt. Lett. 45(24), 6651-6654 (2020).
- <sup>18</sup>B. Chen, Z. Ruan, X. Fan et al., "Low-loss fiber grating coupler on thin film lithium niobate platform," APL Photonics 7(7), 076103 (2022).
- <sup>19</sup>E. Lomonte, F. Lenzini, and W. H. P. Pernice, "Efficient self-imaging grating couplers on a lithium-niobate-on-insulator platform at near-visible and telecom wavelengths," Opt. Express 29(13), 20205-20216 (2021).
- <sup>20</sup>R. Marchetti, C. Lacava, A. Khokhar *et al.*, "High-efficiency grating-couplers: Demonstration of a new design strategy," Sci. Rep. 7(1), 16670 (2017).
- <sup>21</sup>S. Yang, Y. Li, J. Xu *et al.*, "Low loss ridge-waveguide grating couplers in lithium niobate on insulator," Opt. Mater. Express 11(5), 1366-1376 (2021).
- <sup>22</sup>N. V. Sapra, D. Vercruysse, L. Su et al., "Inverse design and demonstration of broadband grating couplers," IEEE J. Select. Top. Quantum Electron. 25(3),
- <sup>23</sup>H. Carfagno, M. A. Guidry, J. Yang et al., "Inverse designed couplers for use in gallium arsenide photonics," ACS Photonics 10(5), 1286-1292 (2023).
- <sup>24</sup>J. Yoon, J. Y. Kim, J. Kim et al., "Inverse design of a Si-based high-performance vertical-emitting meta-grating coupler on a 220 nm silicon-on-insulator platform," Photonics Res. 11(6), 897-905 (2023).